MoS_2 Liquid Cell Electron Microscopy Through Clean and Fast Polymer-Free MoS_2 Transfer

Jiwoong Yang,[†,○] *Moon Kee Choi,*[‡,§,○] *Yuewen Sheng,*[||] *Jaebong Jung,*[⊥] *Karen Bustillo,*[#] *Tongxin Chen,*[||] *Seung-Wuk Lee,*[‡,§] *Peter Ercius,*[#] *Ji Hoon Kim,*[⊥] *Jamie H. Warner,*[||] *Emory M. Chan,*[#] *and Haimei Zheng*[†,▽,*]

[†] Materials Sciences Division, Lawrence Berkeley National Laboratory, Berkeley, California 94720, United States

[‡] Department of Bioengineering and Tsinghua Berkeley Shenzhen Institute, University of California, Berkeley, California 94720, United States

[§] Biological Systems and Engineering Division, Lawrence Berkeley National Laboratory, Berkeley, California 94720, United States

[||] Department of Materials, University of Oxford, 16 Parks Road, Oxford OX1 3PH, United Kingdom

[⊥] School of Mechanical Engineering, Pusan National University, Busan 46241, South Korea

[#] The Molecular Foundry, Lawrence Berkeley National Laboratory, Berkeley, California 94720, United States

[▽] Department of Materials Science and Engineering, University of California, Berkeley, California 94720, United States

[○] J. Yang and M. K. Choi contributed equally to this work.

*E-mail: hmzheng@lbl.gov

ABSTRACT

Two dimensional (2D) materials have found various applications because of their unique physical properties. For example, graphene has been used as the electron transparent membrane for liquid cell transmission electron microscopy (TEM) due to its high mechanical strength and flexibility, single-atom thickness, chemical inertness, etc. Here, we report using 2D MoS_2 as a functional substrate as well as the membrane window for liquid cell TEM, which is enabled by our facile and polymer-free MoS_2 transfer process. This provides the opportunity to investigate the growth of Pt nanocrystals on MoS_2 substrates, which elucidates the formation mechanisms of such heterostructured 2D materials. We find that Pt nanocrystals formed in MoS_2 liquid cells have a strong tendency to align their crystal lattice with that of MoS_2, suggesting a van der Waals epitaxial relationship. Importantly, we can study its impact on the kinetics of the nanocrystal formation. The development of MoS_2 liquid cells will allow further study of various liquid phenomena on MoS_2, and the polymer-free MoS_2 transfer process will be implemented in a wide range of applications.

KEYWORDS

liquid cell electron microscopy, nanocrystal formation, MoS_2, heterostructures, polymer-free transfer

Liquid cell transmission electron microscopy (TEM), which allows imaging through liquids with high spatial and millisecond temporal resolution, has enabled the study of dynamic phenomena in liquids, ranging from nanoscale crystallization[1-5] to transformation,[6-10] self-assembly,[11-14] electrochemical,[15-17] and biological process.[18,19] Recent application of 2D materials, such as graphene as the membrane window for liquid cells,[20-27] has significantly enhanced the image contrast and spatial resolution by reducing electron beam scattering during imaging.[28] Indeed, graphene has been utilized as an excellent membrane material for conventional TEM[29,30] due to its high thermal/electrical conductivity,[31] chemical inertness,[32] impermeability for small molecules,[33] high mechanical strength and flexibility.[34] Currently, the applications of 2D materials for liquid cell TEM have mostly focused on graphene[19-27,35-38] or graphene oxide[39] and their roles are mostly limited to being the encapsulating material or mechanical support. Exploration of other 2D materials – that is not inert for various reactions – as the functional membranes as well as the support for liquid cell TEM will allow the investigations of liquid reactions occurring on the 2D materials, which is significant for the study of formation mechanisms of heterostructured 2D materials.

Heterostructured 2D materials have emerged as an important class of materials offering unique properties due to synergistic effects between 2D materials and the nanomaterials counterpart with various dimensionalities (0D, 1D, and 2D).[40-47] There have been tremendous efforts devoted to the synthesis and characterization of various forms of 2D heterostructures. Among them, heterostructures composed of MoS_2 and noble metal nanoparticles have attracted a lot of attention due to their enhanced catalytic performance.[48-51] It is known that the properties of heterostructured 2D materials are highly sensitive to their atomic structures such as the relative crystal orientation of the constituent materials.[52,53] Consequently, understanding and ultimately controlling noble metal nanoparticle formation on 2D substrates is of key importance in order to fully exploit them for further applications. Previous studies have been

conducted mostly by *ex situ* structure characterization or *in situ* heating experiments under high vacuum.[54-56] The development of MoS_2 liquid cell TEM will enable the direct real-time observation of nanoparticle formation on the 2D MoS_2 substrates and thus, it is highly desirable.

A clean, effective and reproducible transfer process is one of the important prerequisites for practical applications of 2D materials that are usually grown on bulk inorganic substrates by chemical vapor deposition (CVD) methods.[57-63] In order to transfer the 2D materials onto target substrates, spin-cast polymer layers have been employed to protect them from mechanical damage during the transfer process.[64-69] However, it is difficult to completely remove the protection layer, and the polymer residues may deteriorate the optical, electrical, electrochemical, or mechanical properties of the 2D materials.[70-74] For liquid cell TEM, the organic residues may introduce various side-reactions and significantly interrupt the imaging.[35-38,75,76] Polymer-free transfer methods have been well developed for graphene[77-79] since the CVD-substrate (Cu) can be easily etched under mild conditions without introducing significant mechanical damage or deformation to the graphene.[19-27, 35-38,79] However, transition metal chalcogenides, such as MoS_2, are usually grown on SiO_2/Si wafers. Harsh reaction conditions (e.g., high temperature alkaline solutions or high-energy ultrasonic processes) are required to remove the SiO_2/Si substrates, which can damage the 2D films.[80-84] Thus, the development of an efficient polymer-free transfer for MoS_2 has been a challenging goal.

Here, we report the development of MoS_2 liquid cells through a fast and polymer-free transfer process for *in situ* TEM studies of Pt nanocrystal growth on MoS_2. The selective etching of the interfacial SiO_2 layer between the MoS_2 and the Si wafer effectively reduces mechanical damage, resulting in high-yield transfer. The transferred MoS_2 is used in liquid cells as the functional substrate to investigate Pt nanocrystal formation on MoS_2 through *in situ* TEM. This reveals a van der Waals epitaxial relationship between Pt nanocrystals and MoS_2, which significantly affects the nanocrystal growth. Our work demonstrates a facile and clean

transfer method for MoS_2 and facilitates the fundamental understanding of the 2D heterostructure formation.

The polymer-free MoS_2 transfer procedure for *in situ* liquid cell TEM is shown in Figure 1a (See Methods 1.1, 1.2, Figures S1–S3 in the Supporting Information (SI) for experimental details). Quantifoil carbon grids with regular arrays of holes (diameter: ~1.2 μm or ~2.0 μm) are used as target substrates, which allows the application and further characterization of the regions of free standing transferred-MoS_2 sheets. We directly attached the Quantifoil carbon TEM grids on a $MoS_2/SiO_2/Si$ sample without polymer protection layers and used HF to selectively etch the interfacial SiO_2 layer. The MoS_2 sheet was then transferred onto the TEM grid. Scanning electron microscopy (SEM) images of the MoS_2-transferred TEM grids show high coverage of the Quantifoil holes with MoS_2 (Figure 1b, Figures S4, and S5 in SI) regardless of window size (average transfer yields of ~96% and ~91% for the hole size of ~1.2 μm and ~2.0 μm, respectively).

For comparison, we also carried out MoS_2 transfer with the conventional method using KOH etching (See Method 1.2 in SI for experimental details). The gaseous byproducts (H_2) of KOH etching[80-82] can easily damage the MoS_2 sheets. Therefore, the polymer layer is essential to protect the MoS_2 sheets from damage during the conventional transfer process. With polymer protection, a high transfer yield (~95%) is achieved (Figure 1b). However, the complete removal of polymer residues is challenging (Figure S6 in SI), which would be problematic for further applications in liquid cell TEM, due to the poor visibility and undesirable side-reactions induced by the polymer residues during imaging. KOH etching without the polymer protection layer leads to a very low transfer yield (~10%), and the most of membranes are perforated (Figure 1b and Figure S7 in SI).

Theoretical analysis based on finite element method (FEM) simulations validates the high transfer yield of our polymer-free MoS_2 transfer process (See the Method 1.3 in SI for details).

First, we test the role of the target substrate against bending stress. Figure 1c shows the representative stress distribution across MoS_2 sheets (3-layers, ~2-nm-thick) during the etching process with/without the prelaminated target substrate. The maximum applied stress on the MoS_2 sheets attached to the substrate (carbon/gold layer or carbon layer) is more than one order of magnitude lower than that of freestanding MoS_2 sheets under the same applied pressure (Figure 1c and Figure S8 in SI). This implies that the target substrates can effectively act as a protecting layer. Second, FEM calculations estimate the mechanical impact of H_2 bubble generation on MoS_2 sheets floating in the etching solution (Figure 1d and Figure S9 in SI). When bubbles are trapped under MoS_2 sheets, they can cause local stretching of the freestanding MoS_2 sheets. Especially at the edge of the bubbles, the local stress is significant regardless of the bubble size. This suggests that the vigorous bubble generation during the KOH etching process with the relatively long reaction time (tens of minutes) will likely break MoS_2 sheets. In addition, our selective etching reaction takes a very short reaction time (< ~1 sec), which is 1,000 times shorter than that of the conventional KOH etching (Figure S10 in SI). This also helps to minimize the chance of mechanical damage to MoS_2 during the etching process.

Figure 2a shows a representative low-resolution TEM image of the MoS_2-transferred Quantifoil TEM grid (see Method 1.5 in SI). High-resolution TEM images of the two different freestanding MoS_2 region reveal the clean surface with the atomic structure of MoS_2 (Figure 2b,c). A fast Fourier transform (FFT) of the TEM image displays hexagonally arranged spots (d = 0.27 nm), corresponding to the MoS_2 {100} lattice (Figure 2d).[56] A set of the spots corresponding to the MoS_2 {110} lattice planes (~0.17 nm) and higher order spots are also shown in the FFT pattern. Strikingly, with the clean MoS_2 surface, high-resolution TEM images of MoS_2 can be easily obtained without post-image processing or an advanced TEM such as one with aberration-correction or direct electron detection. A TEM image obtained at

a broken region of the film indicates that the MoS_2 used in this study is 2–4 layers thick (Figure S11 in SI). Furthermore, our clean transfer process can be applied to produce multiply stacked MoS_2 structures. TEM images of the stacked structures exhibit Moiré patterns according to the rotational alignment of MoS_2 sheets (Figure S12 in SI).

We further characterize the MoS_2 sheets using Raman spectroscopy. Figure 2e shows the Raman spectra of MoS_2 before (i.e. $MoS_2/SiO_2/Si$) and after (i.e. MoS_2-transferred grids) the transfer process. Both spectra clearly exhibit the characteristic peaks of MoS_2 (E_{2g}^1 mode at ~384 cm^{-1} and A_{1g} mode at ~407 cm^{-1}) without noticeable differences.[85-87] A slight stiffening of the A_{1g} mode can be attributed to the substrate (SiO_2/Si) effect.[86,87] Since Raman spectra of 2D materials are highly related to their structure,[88] these experimental results confirm that the structure of the MoS_2 is well maintained during the transfer process.

We fabricated MoS_2 TEM liquid cells to study Pt nanocrystal formation on MoS_2. The Pt nanocrystal growth solution can be successfully encapsulated between MoS_2- and graphene-transferred grids for TEM imaging (Figure 3a and Method 1.4 in SI). Low-resolution TEM images show that the liquid pockets containing Pt nanocrystals resemble a pseudo-rectangular shape (Figure 3b and Figure S13 in SI). The formation of gas bubbles in the liquid pockets, which are produced by the solvent radiolysis by the electron beam,[76,89] supports the successful encapsulation of liquid samples in MoS_2 liquid cells. The length (the longer axis) and the width (the shorter axis) of the liquid pockets are in the range of several hundreds of nanometers and several tens of nanometers, respectively (Figure 3c,d). The aspect ratio (length/width) of the liquid pockets is large (3–8) as shown in the histogram in Figure S14 in SI. The formation of the anisotropic liquid pockets with pseudo-rectangular shape is very different from previous studies using graphene liquid cells with a similar Pt growth solution, where the liquid pockets are highly irregular (Figure S15 in SI). It is worth mentioning that MoS_2 liquid cells obtained

by the conventional transfer process using polymer protection layers show significant carbon

contamination under the electron beam exposure (Figure S16 in SI), which limits any reliable liquid TEM study.

We further analyze TEM images of the liquid pockets (Figure 3e-l) to determine the distribution of MoS_2 grains around the liquid pockets (See the Method 1.5 in SI). FFT patterns of each whole image exhibits several sets of hexagonally arranged spots corresponding to the MoS_2 lattice (Figure 3f,j). The multiple sets of spots with different rotations suggest the co-existence of the different MoS_2 grains, which is common in CVD-grown multilayer-2D materials. We perform FFT analysis to determine the position and orientations of each grain. The grain distribution is highlighted by the color mapping in the TEM images (Figure 3e,i) and the representative high-resolution masked inverse FFT images are displayed in Figure 3g,h and Figure 3k,l. TEM images without color-mapping and additional masked inverse FFT images acquired from sub-sets of each grain are presented in Figures S17 and S18 in SI. We find that the liquid pockets tend to form between different grains of MoS_2. This is likely due to the different surface properties at the defect sites (grain boundary).[37] Other factors, such as membrane bulging[90] which is also expected to be significant at grain boundaries because of the low mechanical strength, may also affect the liquid distribution.

The successful fabrication of MoS_2 liquid cells provides the opportunity to investigate Pt nanocrystal formation on the MoS_2 with *in situ* liquid cell TEM. Because the growth of Pt nanocrystals has been well studied using traditional *in situ* liquid cell TEM,[1,20,22] we can directly compare experimental results. This will facilitate our fundamental understanding on formation mechanisms of the heterostructures based on 2D MoS_2. The formation of Pt nanocrystals in MoS_2 liquid cells is observed by low-resolution *in situ* TEM imaging (Figure S19 and Movie S1 in SI) and energy dispersive X-ray spectroscopy (Figure S20 in SI). Most Pt nanocrystals are formed within a short period of time (less than 10 sec) after initial exposure to the electron beam. As the reaction proceeds, the growth of nanocrystals results in an

increased image contrast. The Pt nanocrystals show a narrow size distribution with an average diameter of ~2.5 nm (standard deviation of ~0.3 nm, Figure S21 in SI).

High-resolution *in situ* TEM images (Figure 4a and Movie S2) reveal the growth trajectories of individual Pt nanocrystals in MoS_2 liquid cells, showing two representative populations of nanocrystals. One nanocrystal (marked as NC1) appears within ~10 sec and the other nanocrystal (marked as NC2) is formed much later after ~50 sec. This is different from previous observations indicating that most nanocrystals are formed concurrently with a burst nucleation.[91,92] Additional high-resolution *in situ* TEM data show consistent results (Figures S22, S23, and Movie S3 in SI) in that there are two populations of Pt nanocrystals corresponding to the two different formation times. In addition, the translational and rotational motions of Pt nanocrystals are suppressed during growth (Figure 4b), which is in contrast with previous observations that small Pt nanocrystals (~2–3 nm) actively move and rotate in graphene liquid cells (Figure S24 and Movie S4 in SI) under similar experimental conditions (i.e. with the similar solvent and electron beam intensity).[20,22] This comparison implies that the MoS_2 sheets strongly interact with Pt nanocrystals, which will be discussed further below.

The FFT image of the first frame (t_0) of Figure 4a exhibits hexagonally arranged spots corresponding to MoS_2 {100} lattice spacing (Figure 4c). As Pt nanocrystals appear in the *in situ* TEM images (Figure 4a), we can observe the emergence of additional spots in the FFT patterns (marked with white circles in Figure 4d,e). The observed lattice fringes for NC1 and NC2 correspond to Pt (111) and Pt (002) planes, respectively, and the measured lattice parameters (Pt (111): 2.30 Å and Pt (200): 1.95 Å) are similar to those of the bulk crystals (Pt (111): 2.27 Å and Pt (200): 1.96 Å).[93] Strikingly, the spots for Pt (111) of NC1 are aligned with those of MoS_2 (100) with a slight misorientation (< 5°) (Figure 4d,f). Additional high-resolution *in situ* TEM data show the consistent orientation relationship between the Pt [111] direction and one of the MoS_2 <100> directions (Figures S22 and S23b in SI); there appears to be no

obvious relationship for Pt [002] (Compare Figure 4e,f, and Figures S22, S23c in SI). We further analyze more Pt nanocrystals grown on MoS_2 and the most of them show the Pt (111) and (002) lattice. The relative crystal orientations between Pt nanocrystals (Pt [111] and Pt [002] directions) and MoS_2 (one of the MoS_2 <100> directions) are measured (Figure 4g, Figures S25, and S26 in SI). The results from this measurement show that a large fraction of the Pt nanocrystals are aligned with MoS_2 with the relationship of Pt [111] // MoS_2 [100], while the alignment between Pt [002] and MoS_2 crystal directions seems not clear (Figure 4h). The alignment between the Pt [111] direction and one of the MoS_2 <100> directions can be explained by van der Waals epitaxy, which may stabilize the MoS_2-Pt heterostructures. Our results are consistent with previous studies on solution-phase synthesis of Pt nanocrystals on MoS_2, where co-existence of both epitaxially aligned and randomly oriented Pt nanocrystals were observed.[54] Interestingly, the two different growth trajectories of Pt nanocrystals observed (NC1 and NC2) are correlated with the epitaxial relationship between Pt nanocrystals and the MoS_2 substrate. Pt nanocrystals that are epitaxial with MoS_2 (NC1 in Figure 4a and NC3 in Figure S22 in SI) are formed earlier than those with random orientation (NC2 in Figure 4a and NC4 in Figure S22 in SI). This observation suggests that the reduced energy barrier for heterogenous nucleation of Pt nanocrystals on MoS_2 with the van der Waals epitaxy may accelerate the nanocrystal formation.[40-46,54,56,94,95] It is worthwhile to mention that Pt nanocrystals in graphene liquid cells are known to freely rotate,[20,22] and thus do not show orientational relationship. This highlights the importance of the development of MoS_2 liquid cells to study interactions of nanocrystals with 2D materials.

In summary, we have developed an efficient polymer-free MoS_2 transfer method and have showcased the MoS_2 liquid cell electron microscopy with the study of Pt nanocrystal formation on MoS_2. Polymer-free MoS_2 transfer is achieved by the selective etching of the interfacial SiO_2 layer. FEM analysis supports that our polymer-free transfer method can greatly reduce

mechanical damage on the MoS_2, resulting in a high transfer yield. The resulting clean MoS_2 surface is useful for fundamental studies and diverse applications. Our liquid cell TEM study of Pt nanocrystal formation on MoS_2 shows that the [111] direction of Pt nanocrystals has the strong tendency to align with one of the <100> directions of MoS_2. This suggests that there exists a van der Waals epitaxial relationship between Pt nanocrystals and the supporting MoS_2 sheet, which heavily influences the nanocrystal formation kinetics. Our study offers a new prototype to reveal dynamic processes in liquid on 2D materials and provides an effective method for polymer-free transfer of MoS_2, which is potentially applicable to a wide range of investigations.

ASSOCIATED CONTENT

Supporting Information

The Supporting Information is available free of charge on the ACS Publications website at DOI:

Experimental methods, schematic illustrations, SEM images, FEM simulation results, and additional TEM analysis data (PDF)

In situ TEM Movie S1–S4 (AVI)

AUTHOR INFORMATION

Corresponding Author

*E-mail: hmzheng@lbl.gov (H.Z.)

Author Contributions

J.Y. and M.K.C. contributed equally to this work.

Notes

The authors declare no competing financial interest.

ACKNOWLEDGMENT

This work was supported by the U.S. Department of Energy, Office of Science, Office of Basic Energy Sciences, Materials Sciences and Engineering Division, under Contract No. DE-AC02-05CH11231 within the insitu TEM program (KC22ZH). Work at the Molecular Foundry was supported by the Office of Science, Office of Basic Energy Sciences, of the U.S. Department of Energy under Contract No. DE-AC02-05CH11231. J.H.K. acknowledges the Basic Science Research Program through the National Research Foundation of Korea (NRF) funded by the Ministry of Science and ICT (Grant No. 2015R1C1A1A01051620). M.K.C. and S.-W.L. were supported by Tsinghua Berkeley Shenzhen Institute Fund.

References

(1) Zheng, H.; Smith, R. K.; Jun, Y.-w.; Kisielowski, C.; Dahmen, U.; Alivisatos, A. P. *Science* **2009**, *324*, 1309–1312.

(2) Nielsen, M. H.; Aloni, S.; De Yoreo, J.J. *Science* **2014**, *345*, 1158–1162.

(3) Woehl, T. J.; Evans, J. E.; Arslan, I.; Ristenpart, W. D., Browning, N. D. *ACS Nano* **2012**, *6*, 8599–8610.

(4) De Yoreo, J. J.; Sommerdijk N. A. J. M. *Nat. Rev. Mater.* **2016**, *1*, 16035.

(5) Sutter, P.; Li, Y.; Argyropoulos, C.; Sutter, E. *J. Am. Chem. Soc.* **2017**, *139*, 6771–6776.

(6) Hauwiller, M. R.; Zhang, X.; Liang, W.-I.; Chiu, C.-H.; Zhang, Q.; Zheng, W.; Ophus,

C.; Chan, E. M.; Czarnik, C.; Pan, M.; Ross, F. M.; Wu, W.-W.; Chu, Y.-H.; Asta, M.; Voorhees, P. W.; Alivisatos, A. P.; Zheng, H. *Nano Lett.* **2018**, *18*, 6427–6433.

(7) Liao, H.-G.; Zherebetskyy, D.; Xin, H.; Czarnik, C.; Ercius, P.; Elmlund, H.; Pan, M.; Wang, L.-W.; Zheng, H. *Science* **2014**, *345*, 916–919.

(8) Sutter, E.; Jungjohann, K.; Bliznakov, S.; Courty, A.; Maisonhaute, E.; Tenney, S.; Sutter, P. *Nat. Commun.* **2014**, *5*, 4946.

(9) Gao, W.; Hou, Y.; Hood, Z. D.; Wang, X.; More, K.; Wu, R.; Xia, Y.; Pan, X.; Chi, M. *Nano Lett.* **2018**, *18*, 7004–7013.

(10) Kim, B. H.; Yang, J.; Lee, D.; Choi, B. K.; Hyeon, T.; Park, J. *Adv. Mater.* **2018**, *30*, 1703316.

(11) Powers, A. S.; Liao, H.-G.; Raja, S. N.; Bronstein, N. D.; Alivisatos, A.P.; Zheng, H. *Nano Lett.* ***2016***, *17*, 15–20.

(12) Lee, W. C.; Kim, B. H.; Choi, S.; Takeuchi, S.; Park, J. *J. Phys. Chem. Lett.* **2017**, *8*, 647–654.

(13) Tan, S. F.; Chee, S. W.; Lin, G.; Mirsaidov, U. *Acc. Chem. Res.* **2017**, *50*, 1303–1312.

(14) Luo, B.; Smith, J. W.; Ou, Z.; Chen, Q. *Acc. Chem. Res.* **2017**, *50*, 1125–1133.

(15) Williamson, M. J.; Tromp, R. M.; Vereecken, P. M.; Hull, R.; Ross, F. M. *Nat. Mater.* **2003**, *2*, 532– 536.

(16) Gu, M.; Parent, L. R.; Mehdi, B. L.; Unocic, R. R.; McDowell, M. T.; Sacci, R. L.; Xu, W.; Connell, J. G.; Xu, P.; Abellan, P.; Chen, X.; Zhang, Y.; Perea, D. E.; Evans, J. E.; Lauhon, L. J.; Zhang, J.-G.; Liu, J.; Browning, N. D.; Cui, Y.; Arslan, I.; Wang, C.-M. *Nano Lett.* **2013**, *13*, 6106–6112.

(17) Zeng, Z.; Zheng, W.; Zheng, H. *Acc. Chem. Res.* **2017**, 50, 1808–1807.

(18) Park, J.; Park, H.; Ercius, P.; Pegoraro, A. F.; Xu, C.; Kim, J. W.; Han, S. H.; Weitz, D. A.; *Nano Lett.* **2015**, *15*, 4737–4744.

(19) Liv, N.; van Oosten Slingeland, D. S.; Baudoin, J. P.; Kruit, P.; Piston, D. W.; Hoogenboom, J. P. *ACS Nano* **2016**, *10*, 265−273.

(20) Yuk, J. M.; Park, J.; Ercius, P.; Kim, K.; Hellebusch, D. J.; Crommie, M. F.; Lee, J. Y.; Zettl, A.; Alivisatos, A. P. *Science* **2012**, *336*, 61–64.

(21) Chen, Q.; Smith, J. M.; Park, J.; Kim, K.; Ho, D.; Rasool, H. I.; Zettl, A.; Alivisatos, A.P. *Nano Lett.* **2013**, *13*, 4556–4561.

(22) Park, J.; Elmlund, H.; Ercius, P.; Yuk, J. M.; Limmer, D. T.; Chen, Q.; Kim, K.; Han, S. H.; Weitz, D. A.; Zettl, A.; Alivisatos, A. P. *Science* **2015**, *349*, 290–295.

(23) Ye, X.; Jones, M. R.; Frechette, L. B.; Chen, Q.; Powers, A. S.; Ercius, P.; Dunn, G.; Rotskoff, G. M.; Nguyen, S. C.; Adiga, V. P.; Zettl, A.; Rabani, E.; Geissler, P. L.; Alivisatos, A. P. *Science* **2016**, *354*, 874–877.

(24) Dahmke, I. N.; Verch, A.; Hermannsdorfer, J.; Peckys, D. B.; Weatherup, R. S.; Hofmann, S.; de Jonge, N. *ACS Nano* **2017**, *11*, 11108–11117.

(25) Nagamanasa, K. H.; Wang, H.; Granick, S. *Adv. Mater.* **2017**, *29*, 1703555.

(26) Kelly, D.; Zhou, M.; Clark, N.; Hamer, M. J.; Lewis, E. A.; Rakowski, A. M.; Haigh, S. J.; Gorbachev, R. V. *Nano Lett.* **2018**, *18*, 1168–1174.

(27) Textor, M.; de Jonge, N. *Nano Lett.* **2018**, *18*, 3313–3321.

(28) de Jonge, N. *Ultramicroscopy* **2018**, *187*, 113–125.

(29) Meyer, J. C.; Girit, C. O.; Crommie, M. F.; Zettl, A. *Nature* **2008**, *454*, 319–322.

(30) Nair, R. R.; Blake, P.; Blake, J. R.; Zan, R.; Anissimova, S.; Bangert, U.; Golovanov, A. P.; Morozov, S. V.; Geim, A. K.; Novoselov, K. S.; Latychevskaia, T. *Appl. Phys. Lett.* **2010**, *97*, 153102.

(31) Bolotin, K. I.; Sikes, K. J.; Jiang, Z.; Klima, M.; Fudenberg, G.; Hone, J.; Kim, P.; Stormer, H. L. *Solid State Commun.* **2008**, *146*, 351– 355.

(32) Aliofkhazraei, M.; Ali, N.; Milne, W. I.; Ozkan, C. S.; Mitura, S.; Gervasoni, J. L. *Graphene science handbook: electrical and optical properties*; CRC Press: Boca Raton, FL, **2016**.

(33) Xu, K.; Cao, P.; Heath, J. R. *Science* **2010**, *329*, 1188–1191.

(34) Lee, C.; Wei, X.; Kysar, J. W.; Hone, J. *Science* **2008**, *321*, 385–388.

(35) Cho, H.; Jones, M. R.; Nguyen, S. C.; Hauwiller, M. R.; Zettl, A.; Alivisatos, A. P. *Nano Lett.* **2017**, *17*, 414–420.

(36) Wang, H.; Nagamanasa, K. H.; Kim, Y.-J.; Kwon, O.-H., Granick, S. *ACS Nano* **2018**, *12*, 8572–8578.

(37) Yang, J.; Alam, S. B.; Yu, L.; Chan, E.; Zheng, H. *Micron* **2019**, *116*, 22–29.

(38) Keskin, S.; de Jonge, N. *Nano Lett.* **2018**, *18*, 7435–7440.

(39) Krueger, M.; Berg, S.; Stone, D.; Strelcov, E.; Dikin, D. A.; Kim, J.; Cote, L. J.; Huang, J.; Kolmakov, A. *ACS Nano* **2011**, *5*, 10047–10057.

(40) Huang, X.; Qi, X.; Boey, F.; Zhang, H. *Chem. Soc. Rev.* **2012**, *41*, 666–686.

(41) Butler, S. Z.; Hollen, S. M.; Cao, L.; Cui, Y.; Gupta, J. A.; Gutiérrez, H. R.; Heinz, T. F.; Hong, S. S.; Huang, J.; Ismach, A. F.; Johnston-Halperin, E.; Kuno, M.; Plashnitsa, V. V.; Robinson, R. D.; Ruoff, R. S.; Salahuddin, S.; Shan, J.; Shi, L.; Spencer, M. G.; Terrones, M.; Windl, W.; Goldberger, J. E. *ACS Nano* **2013**, *7*, 2898–2926.

(42) Geim, A. K.; Grigorieva, I. V. *Nature* **2013**, *499*, 419–425.

(43) Yu, J. H.; Lee, H. R.; Hong, S. S.; Kong, D.; Lee, H.-W.; Wang, H.; Xiong, F.; Wang, S.; Cui, Y. *Nano Lett.* **2015**, *15*, 1031–1035.

(44) Ban, H. W.; Park, S.; Jeong, H.; Gu, D. H.; Jo, S.; Park, S. H.; Park, J.; Son, J. S. *J. Phys. Chem. Lett.* **2016**, *7*, 3627–3635.

(45) Liu, Y.; Weiss, N. O.; Duan, X.; Cheng, H.-C.; Huang, Y.; Duan, X. *Nat. Rev. Mater.* **2016**, *1*, 16042.

(46) Yang, J.; Kim, K.; Lee, Y.; Kim, K.; Lee, W. C.; Park, J. *FlatChem* **2017**, *5*, 50–68.

(47) Woods, J. M.; Jung, Y.; Xie, Y.; Liu, W.; Liu, Y.; Wang, H.; Cha, J. J. *ACS Nano* **2016**, *10*, 2004−2009.

(48) Deng, J.; Li, H.; Xiao, J.; Tu, Y.; Deng, D.; Yang, H.; Tian, H.; Li, J.; Ren, P.; Bao, X. *Energy Environ. Sci.* **2015**, *8*, 1594−1601.

(49) Deng, D.; Novoselov, K. S.; Fu, Q.; Zheng, N.; Tian, Z.; Bao, X. *Nat. Nanotechnol.* **2016**, *11*, 218−230.

(50) Li, H.; Wang, L.; Dai, Y.; Pu, Z.; Lao, Z.; Chen, Y.; Wang, M.; Zheng, X.; Zhu, J.; Zhang, W.; Si, R.; Ma, C.; Zeng, J. *Nat. Nanotechnol.* **2018**, *13*, 411−417.

(51) Li, Y.; Majewski, M. B.; Islam, S. M.; Hao, S.; Murthy, A. A.; DiStefano, J. G.; Hanson, E. D.; Xu, Y.; Wolverton, C.; Kanatzidis, M. G.; Wasielewski, M. R.; Chen, X.; Dravid, V. P. *Nano Lett.* **2018**, *18*, 7104–7110.

(52) Zhang, Y.; Tang, T.-T.; Girit, C.; Hao, Z.; Martin, M. C.; Zettl, A.; Crommie, M. F.; Shen, Y. R.; Wang, F. *Nature* **2009**, *459*, 820–823.

(53) Yankowitz, M.; Xue, J.; Cormode, D.; Sanchez-Yamagishi, J. D.; Watanabe, K.; Taniguchi, T.; Jarillo-Herrero, P.; Jacquod, P.; LeRoy, B. J. *Nat. Phys.* **2012**, *8*, 382–386.

(54) Huang, X.; Zeng, Z.; Bao, S.; Wang, M.; Qi, X.; Fan, Z.; Zhang, H. *Nat. Commun.* **2013**, *4*, 1444.

(55) Li, H.; Wang, S.; Sawada, H.; Han, G. G. D.; Samuels, T.; Allen, C. S.; Kirkland, A. I.; Grossman, J. C.; Warner, J. H. *ACS Nano* **2017**, *11*, 3392–3403.

(56) Wang, S.; Sawada, H.; Chen, Q.; Han, G. G. D.; Allen, C.; Kirkland, A. I.; Warner, J. H. *ACS Nano* **2017**, *11*, 9057–9067.

(57) Kim, K. S.; Zhao, Y.; Jang, H.; Lee, S. Y.; Kim, J. M.; Kim, K. S.; Ahn, J.-H.; Kim, P.; Choi, J.-Y.; Hong, B. H. *Nature* **2009**, *457*, 706–710.

(58) Li, H.; Wu. J.; Huang, X.; Yin, Z.; Liu, J.; Zhang, H. *ACS Nano* **2014**, *8*, 6563–6570.

(59) Akinwande, D.; Petrone, N.; Hone, J. *Nat. Commun.* **2014**, *5*, 5678.

(60) Chang, H.-Y.; Yang, S.; Lee, J.; Tao, L.; Hwang, W.-S.; Jena, D.; Lu, N.; Akinwande, D. *ACS Nano* **2013**, *7*, 5446–5452.

(61) Choi, C.; Choi, M. K.; Liu, S.; Kim, M. S.; Park, O. K.; Kim, J.; Kim, C.; Qin, X.; Lee, G. J.; Cho, K. W.; Kim, M.; Joh, E.; Lee, J.; Son, D.; Kwon, S.-H.; Jeon, N. L.; Song, Y. M.; Lu, N.; Kim, D.-H. *Nat. Commun.* **2017**, *8*, 1664.

(62) Hong, X.; Kim, J.; Shi, S.-F.; Zhang, Y.; Jin, C.; Sun, Y.; Tongay, S.; Wu, J.; Zhang, Y.; Wang, F.; *Nat. Nanotechnol.* **2014**, *9*, 682–686.

(63) Schmidt, H.; Wang, S.; Chu, L.; Toh, M.; Kumar, R.; Zhao, W.; Neto, A. H. C.; Martin, J.; Adam, S.; Özyilmaz, B.; Eda, G. *Nano Lett.* **2014**, *14*, 1909−1913.

(64) Zhan, Y.; Liu, Z.; Najmaei, S.; Ajayan, P. M.; Lou, J. *Small* **2012**, *8*, 966−971.

(65) Zhang, Z.; Du, J.; Zhang, D.; Sun, H.; Yin, L.; Ma, L.; Chen, J.; Ma, D.; Cheng, H.-M.; Ren, W. *Nat. Commun.* **2017**, *8*, 14560.

(66) Suk, J. W.; Kitt, A.; Magnuson, C. W.; Hao, Y.; Ahmed, S.; An, J.; Swan, A. K.; Goldberg, B. B.; Ruoff, R. S. *ACS Nano* **2011**, *5*, 6916–6924.

(67) Lock, E. H.; Baraket, M.; Laskoski, M.; Mulvaney, S. P.; Lee, W. K.; Sheehan, P. E.; Hines, D. R.; Robinson, J. T.; Tosado, J.; Fuhrer, M. S.; Hernandez, S. C.; Walton, S. G. *Nano Lett.* **2012**, *12*, 102–107.

(68) Song, J.; Kam, F.-Y.; Png, R.-Q.; Seah, W.-L.; Zhuo, J.-M.; Lim, G.-K.; Ho, P. K. H.; Chua, L.-L. *Nat. Nanotechnol.* **2013**, *8*, 356–362.

(69) Gao, L.; Ni, G.-X.; Liu, Y.; Liu, B.; Neto, A. H. C.; Loh, K. P. *Nature* **2014**, *505*, 190–194.

(70) Lin, Z.; Zhao, Y.; Zhou, C.; Zhong, R.; Wang, X.; Tsang, Y. H.; Chai, Y. *Sci. Rep.* **2015**, *5*, 18596.

(71) Choi, M. K.; Park, I.; Kim, D. C.; Joh, E.; Park, O. K.; Kim, J.; Kim, M.; Choi, C.; Yang, J.; Cho, K. W.; Hwang, J.-H.; Nam, J.-M.; Hyeon, T.; Kim, J. H.; Kim, D.-H. *Adv. Funct. Mater.* **2015**, *25*, 7109–7118.

(72) Bae, S.; Kim, H.; Lee, Y.; Xu, X.; Park, J.-S.; Zheng, Y.; Balakrishnan, J.; Lei, T.; Kim, H. R.; Song, Y. I.; Kim, Y.-J.; Kim, K. S.; Ozyilmaz, B.; Ahn, J.-H.; Hong, B. H.; Iijima, S. *Nat. Nanotechnol.* **2010**, *5*, 574–578.

(73) Wang, X.; Tao, L.; Hao, Y.; Liu, Z.; Chou, H.; Kholmanov, I.; Chen, S.; Tan, C.; Jayant, N.; Yu, Q.; Akinwande, D.; Ruoff, R. S. *Small* **2014**, *10*, 694–698.

(74) Jung, W.; Kim, D.; Lee, M.; Kim, S.; Kim, J.-H.; Han, C.-S. *Adv. Mater.* **2014**, *26*, 6394–6400.

(75) Abellan, P.; Woehl, T. J.; Parent, L. R.; Browning, N. D.; Evans, J. E.; Arslan, I. *Chem. Commun.* **2014**, *50*, 4873–4880.

(76) Woehl, T. J.; Abellan, P. *J. Microsc.* **2017**, *265*, 135–147.

(77) Regan, W.; Alem, N.; Alemán, B.; Geng, B.; Girit, C-.; Maserati, L.; Wang, F.; Crommie, M.; Zettl, A. *Appl. Phys. Lett.* **2010**, *96*, 113102.

(78) Lin, W.-H.; Chen, T.-H.; Chang, J.-K.; Taur, J.-I; Lo, Y.-Y.; Lee, W.-L.; Chang, C.-S.; Su, W.-B.; Wu, C.-I. *ACS Nano* **2014**, *8*, 1784–1791.

(79) Zhang, J.; Lin, L.; Sun, L.; Huang, Y.; Koh, A. L.; Dang, W.; Yin, J.; Wang, M.; Tan, C.; Li, T.; Tan, Z.; Liu, Z.; Peng, H. *Adv. Mater.* **2017**, *29*, 1700639.

(80) Tsai, M.-L.; Su, S.-H.; Chang, J.-K.; Tsai, D.-S.; Chen, C.-H.; Wu, C.-I; Li, L.-J.; Chen, L.-J.; He, J.-H. *ACS Nano* **2014**, *8*, 8317–8322.

(81) Gurarslan, A.; Yu, Y.; Su, L.; Yu, Y.; Suarez, F.; Yao, S.; Zhu, Y.; Ozturk, M.; Zhang, Y.; Cao, L. *ACS Nano* **2014**, *8*, 11522–11528.

(82) Yu, H.; Liao, M.; Zhao, W.; Liu, G.; Zhou, X. J.; Wei, Z.; Xu, X.; Liu, K.; Hu, Z.; Deng, K.; Zhou, S.; Shi, J.-A.; Gu, L.; Shen, C.; Zhang, T.; Du, L.; Xie, L.; Zhu, J.; Chen, W.;

Yang, R.; Shi, D.; Zhang, G. *ACS Nano* **2017**, *11*, 12001–12007.

(83) Ma, D.; Shi, J.; Ji, Q.; Chen, K.; Yin, J.; Lin, Y.; Zhang, Y.; Liu, M.; Feng, Q.; Song, X.; Guo, X.; Zhang, J.; Zhang, Y.; Liu, Z. *Nano Res.* **2015**, *8*, 3662–3672.

(84) Lee, Y.-H.; Yu, L.; Wang, H.; Fang, W.; Ling, X.; Shi, Y.; Lin, C.-T.; Huang, J.-K.; Chang, M.-T.; Chang, C.-S.; Dresselhaus, M.; Palacios, T.; Li, L.-J.; King, J. *Nano Lett.* **2013**, *13*, 1852–1857.

(85) Jimenez, S.; Sandoval, D.; Yang, D. Frindt, R. F.; Irwin, J. C. *Phys. Rev. B* **1991**, *44*, 3955–3962.

(86) Li, H.; Zhang, Q.; Yap, C. C. R.; Tay, B. K.; Edwin, T. H. T.; Olivier, A.; Baillargeat D. *Adv. Funct. Mater.* **2012**, *22*, 1385–1390.

(87) Zhang, X.; Qiao, X.-F.; Shi, W.; Wu, J.-B.; Jiang, D.-S.; Tan, P.-H. *Chem. Soc. Rev.* **2015**, *44*, 2757–2785.

(88) Ferrari, A. C.; Meyer, J. C.; Scardaci, V.; Casiraghi, C.; Lazzeri, M.; Mauri, F.; Piscanec, S.; Jiang, D.; Novoselov, K. S.; Roth, S.; Geim, A. K. *Phys. Rev. Lett.* **2006**, *97*, 187401.

(89) Grogan, J. M.; Schneider, N. M.; Ross, F. M.; Bau, H. H. *Nano Lett.* **2014**, *14*, 359–364.

(90) de Jonge, N.; Peckys, D. B.; Kremers, G. J.; Piston, D. W. *Proc. Natl. Acad. Sci USA* **2009**, *106*, 2159–2164.

(91) Sugimoto, T. *Adv. Colloid Interfac. Sci.* **1987**, *28*, 65–108.

(92) Kwon, S. G.; Hyeon, T. *Small* **2011**, *7*, 2685–2702.

(93) Wyckoff, R. W. G. *Crystal structures*; 2nd ed.; Interscience: New York. 1963.

(94) Lee, W. C., Kim, K., Park, J., Koo, J., Jeong, H. Y., Lee, H., Weitz, D. A., Zettl, A., Takeuchi, S. *Nat. Nanotechnol.* **2015**, *10*, 423–428.

(95) Jang, J.; Lee, Y.; Yoon, J.-Y.; Yoon, H. H.; Koo, J.; Choe, J.; Jeon, S.; Sung J.; Park, J.; Lee, W. C.; Lee, H.; Jeong, H. Y.; Park, K.; Kim. K. *Nano Lett.* **2018**, *18*, 6214–6221.

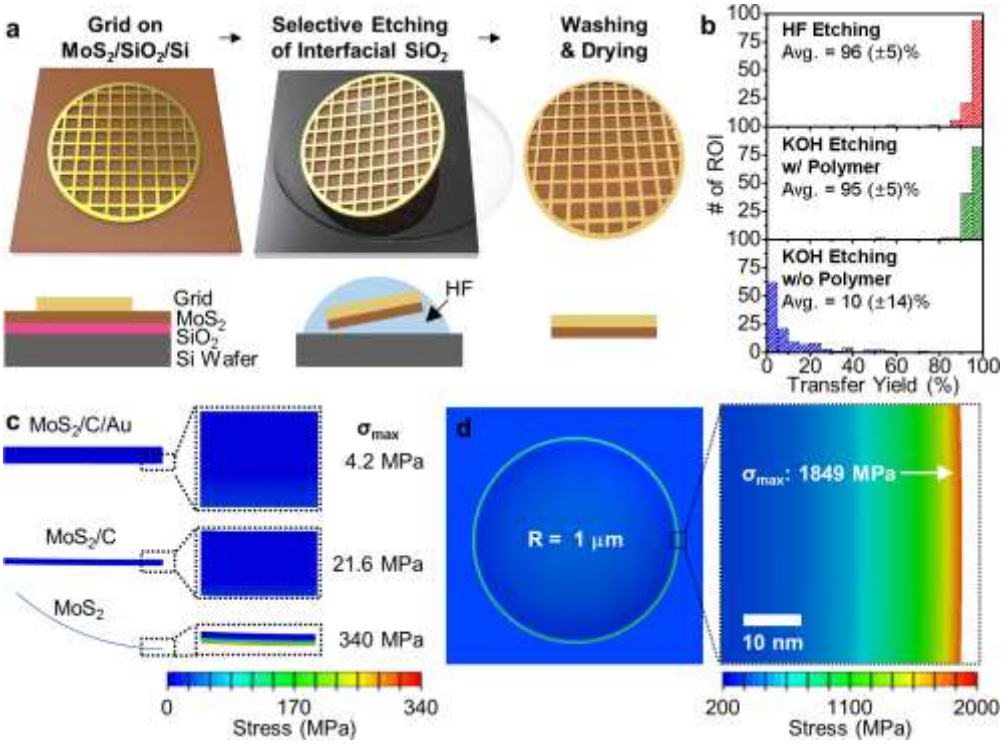

Figure 1. Polymer-free transfer process of MoS_2. (a) Schematic illustration of our polymer-free transfer method: (i) attachment of TEM grids on $MoS_2/SiO_2/Si$, (ii) selective etching of interfacial SiO_2, and (iii) washing/drying. (b) Histograms showing the distribution of the transfer yield within the region of interest (ROI) according to the transfer methods. 120 ROIs were used for each histogram and each ROI contains ~100 Quantifoil holes. (c) FEM simulations of the stress distribution on MoS_2, MoS_2/carbon, and MoS_2/carbon/gold layered structures during bending by external forces. The thickness of MoS_2, carbon, gold layers are 2 nm, 10 nm, and 20 nm, respectively for the simulation. The results are obtained under the same external pressure (5×10^{-5} Pa). The maximum stress is noted for each case. The images are drawn in scale. (d) FEM simulation of the stress distribution on a freestanding MoS_2 sheet by stretching due to the bubble attachment. The result is obtained for MoS_2 trapping a bubble with the radius of 1 μm. The additional simulation results are shown in Figures S8 and S9 in SI.

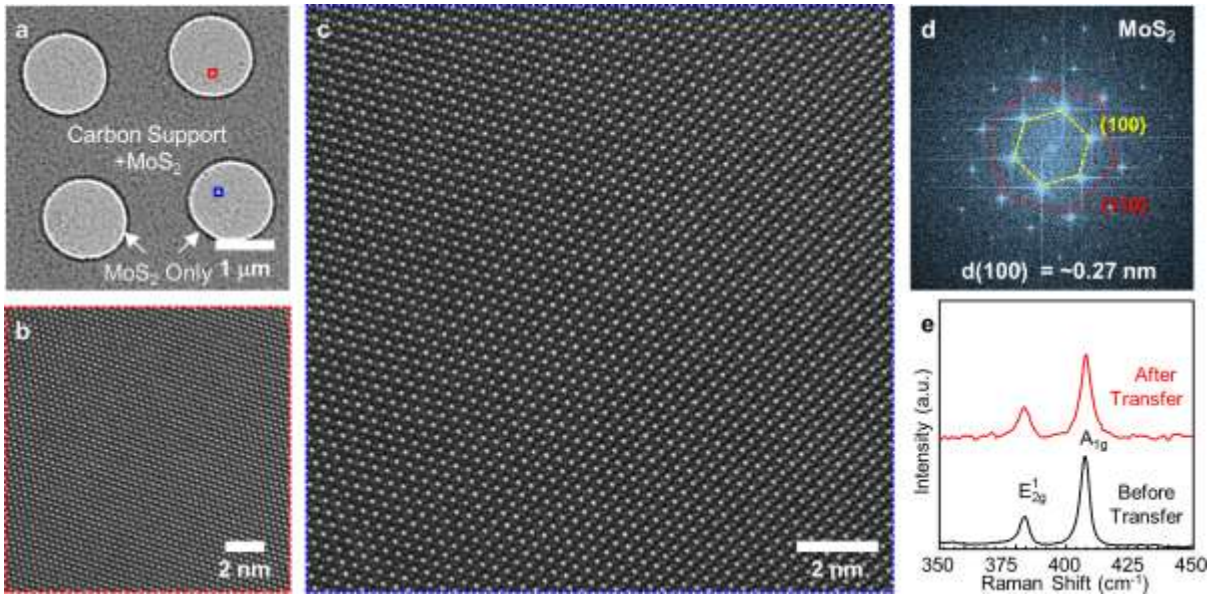

Figure 2. Characterization of polymer-free transferred MoS_2. (a) Low-resolution TEM image showing the support and holes of a MoS_2-transferred TEM grid. A MoS_2 membrane is transferred on the carbon support with ~1.2 μm diameter holes. (b,c) High-resolution TEM images of transferred MoS_2. Crystal orientations of MoS_2 in the panel (b) and (c) are slightly different, because of the polycrystalline nature of multilayer MoS_2. The images are obtained from boxed area of the panel (a). (d) The FFT image of the panel (c). The data were acquired using a Tecnai at 200 kV. (e) Raman spectra of MoS_2 on SiO_2/Si (black, before the transfer process) and MoS_2 on a TEM grid (red, after the transfer process).

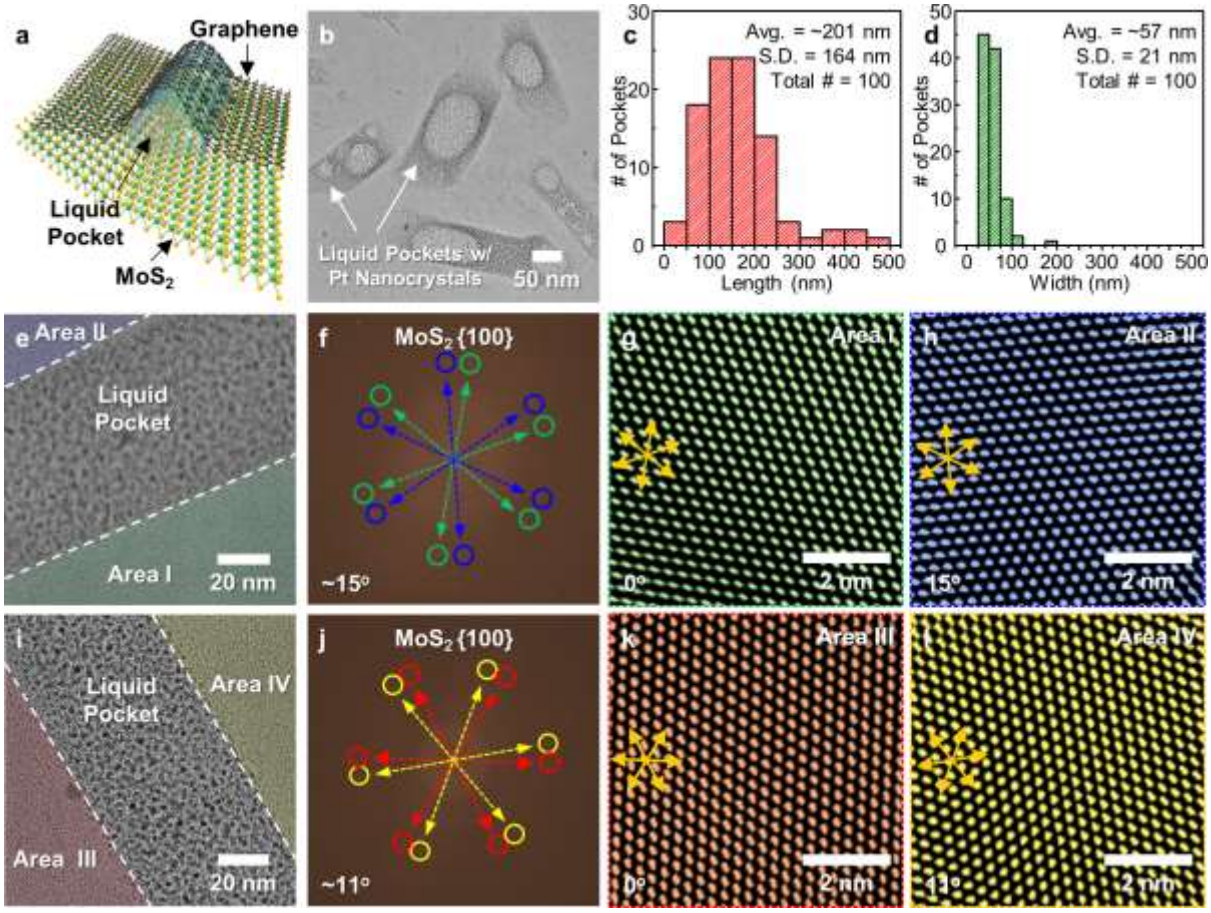

Figure 3. Liquid pocket formation in MoS_2 liquid cells. (a) Schematic illustration of the part of a MoS_2 liquid cell encapsulating liquid solution. (b) Low-resolution TEM image showing the overall morphology of the liquid pockets. (c,d) Histograms showing the distribution of (c) the length and (d) width of liquid pockets. (e) False-colored TEM image of a liquid pocket and (f) the corresponding FFT with the circled spots and arrows indicating different MoS_2 grains. The areas with different MoS_2 grains are highlighted by green (area I) and blue (area II). (g,h) Representative high-resolution masked inverse FFT images of area I and II. The orange arrows indicate the MoS_2 <100> directions. Area I and area II are related to green and blue circled spots in the FFT image, respectively. (i) Another false-colored TEM image and (j) the corresponding FFT. The areas with the different MoS_2 grains are highlighted by red (area III) and yellow (area IV). (k,l) Representative high-resolution masked inverse FFT images of area III and IV. The orange arrows indicate the MoS_2 <100> directions. Area III and area IV are related to red and yellow circled spots in the FFT image, respectively. The liquid cell TEM data were acquired using an aberration-corrected ThemIS at 300 kV.

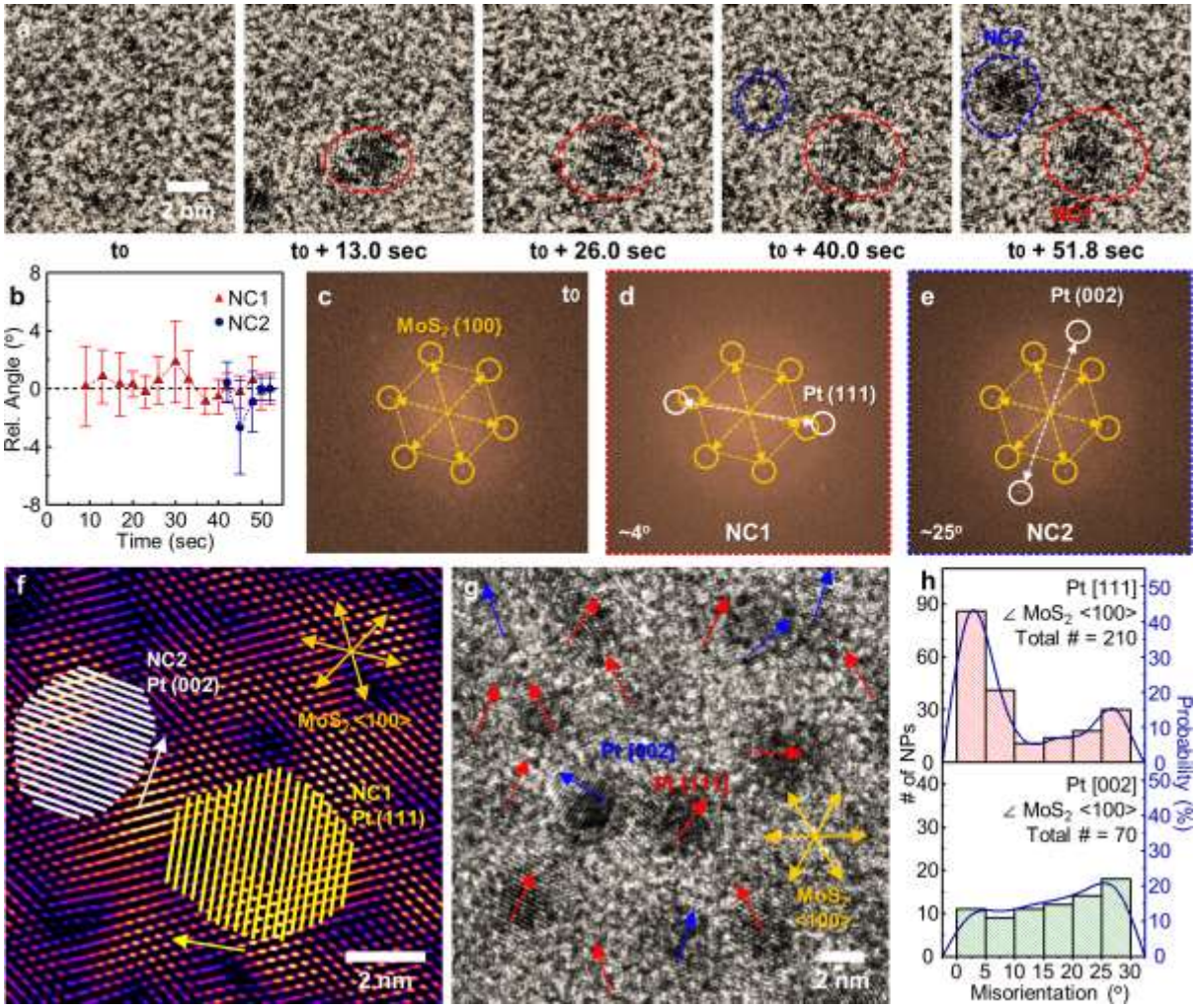

Figure 4. Formation of Pt nanocrystals on MoS_2. (a) A time-series of high-resolution *in situ* TEM images showing the formation of individual Pt nanocrystals. The corresponding movie is displayed in Movie S2. (b) A plot showing the relative orientation of Pt nanocrystals as a function of the time. The orientation at the last time frame is set as 0° for the both nanocrystals. (c–e) FFT of the first image (t_0) and NC1 and NC2 in the last frame (t_0 + 51.8 sec). (f) An image showing the relative crystalline orientation of Pt nanocrystals and MoS_2. The image is obtained by overlapping the lattice fringes of Pt nanocrystals on inverse FFT image (a fire color lookup table) of MoS_2 in the final frame (t_0 + 51.8 sec). (g) TEM image showing as-grown Pt nanocrystals where the orientation of Pt [111] and Pt [002] are marked with blue and red arrows, respectively. MoS_2 <100> directions are indicated by the orange arrows. (h) Histograms showing the misalignment angles between Pt nanocrystals (Pt [111] and Pt [002] directions) and MoS_2 (one of the MoS_2 <100> directions). The data are acquired from 210 nanocrystals for Pt [111] and 70 nanocrystals for Pt [002]. The liquid cell TEM data were acquired using an aberration-corrected ThemIS at 300 kV.
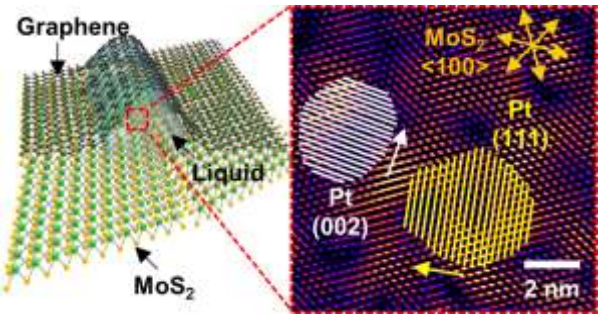
Table of Contents Graphic